International Journal of Impact Engineering 144 (2020) 103647

Contents lists available at ScienceDirect

International Journal of Impact Engineering

journal homepage: www.elsevier.com/locate/ijimpeng

Failure analysis of reinforced concrete slab under impact loading using a novel numerical method

Jianguo Ning, Fanlin Meng, Tianbao Ma, Xiangzhao Xu*

State Key Laboratory of Explosion Science and Technology, Beijing Institute of Technology, Beijing 100081, China

ARTICLE INFO

Keywords:
Reinforced concrete
Impact loading
Coupled Eulerian-Lagrangian method
Numerical simulation

ABSTRACT

Failure analyses of reinforced concrete slabs under impact loading are essential to evaluate the impact resistance of structures accurately; further, these analyses help reasonably design and construct engineering structures. In this paper, we propose a novel three-dimensional (3D) coupled Eulerian-Lagrangian method to simulate projectile penetration into the reinforced concrete slab. In this method, the entire computational domain is covered with Eulerian cells. The reinforcing bar is also covered with Lagrangian particles to avoid numerical oscillations. The physical quantities of the Eulerian cells and Lagrangian particles are mapped to each other by their topological relationships. Different materials do not embed owing to the combination of the fixed cells and single-valued mapping. Numerical simulations of projectile penetration into the concrete slab are compared with the corresponding experimental data and previous numerical results to verify the effectiveness of the coupled Eulerian-Lagrangian method. Then, the deformation history of the reinforcing bar, and the influence of initial penetration velocity, reinforcing bar, and the uniaxial compressive strength and thickness of concrete on the penetration performance are conducted. Numerical results demonstrate that the 3D Eulerian-Lagrangian method can effectively simulate projectile penetration into the reinforced concrete slab.

1. Introduction

Concrete material is one of the most widely used materials in structural engineering, and has a history of application for centuries. Reinforcement bars or racks are implanted into concrete to form a sturdy construction material with enhanced compressive and tensile strength. Currently, many special engineering structures adopt concrete or reinforced concrete in civil and military applications [1–3]. Therefore, the research on projectile penetration into the reinforced concrete has received considerable attention. Failure analyses of reinforced concrete slab under impact loading are significant for an accurate evaluation of the impact resistance of structures and their design and construction [4,5].

Numerical simulations have become an important method for solving complex problems in engineering applications and scientific computing [6–8]. They play a valuable role in providing tests and examinations for theories, offering insights into complex physics, and assisting in the interpretation and the discovery of new phenomena [9,10]. In addition, numerical simulations can break through the limitations of experimental and theoretical research and can study the variation laws of the physical quantities with different initial conditions. Furthermore, it offers high efficiency with low cost than experiment approaches. Numerical simulation of projectile penetration into the reinforced concrete slab is challenging because of material large deformation, multi-material interface treatment, high pressure, high strain rate, and strong discontinuity. Coupled with an appropriate interface capturing algorithm, the Eulerian method is quite attractive for penetration problems, as it allows boundaries to flow through a fixed cell while computing the flow field on the fixed cell. However, the material deformation needs to be accurately monitored, often by using the Lagrangian method for the deformation of the reinforcing bar during the projectile penetration into the reinforced concrete slab.

Researchers used various techniques for the numerical simulation of projectile penetration into the concrete slab. grdh [11] simulated a projectile penetration of the fiber reinforced concrete slab at the initial impact velocity 1500 m/s using the LS-DYNA with the Lagrangian method and preliminary obtained the process of projectile penetration into reinforced concrete. Subsequently, Huang et al. [12] further conducted a numerical study on a projectile penetration of the reinforced concrete slab. The crater diameters on the front and back surfaces of the concrete slab and the residual velocities of projectiles were obtained, and the influence of the reinforcement on the perforation of concrete slab was also studied. Tham [13] used the AUTODYN with the Eulerian method to simulate the maximum depth of penetration and the radial

* Corresponding author.
E-mail address: 7520180029@bit.edu.cn (X. Xu).

https://doi.org/10.1016/j.ijimpeng.2020.103647
Received 15 October 2019; Received in revised form 29 April 2020; Accepted 10 June 2020
Available online 11 June 2020
0734-743X/

stress-time response of the concrete slab. Ning et al. [6] proposed a multi-material Eulerian method for solving the 3D explosion and impact problems. Kapahi et al. [14] presented a three-dimensional Eulerian sharp interface using the Cartesian grid technique for simulating high-speed multi-material impact problems. Thus, both the Eulerian and Lagrangian methods can be used to simulate the penetration problem. However, dealing with penetration only by a single method is ineffective. The Lagrangian method can accurately tracks the material deformation process, but requires the remap framework to deal with the mesh distortion problem. Conversely, the Eulerian method can efficiently deal with the mesh distortion problems using a fixed mesh, but cannot accurately track the material deformation process. Subsequently, the coupled methods [15] are conducted to incorporate the advantages of the Eulerian and Lagrangian methods and effectively implement the numerical simulation of the penetration problem. Material point method (MPM) [16] is one typical type of the coupled methods. In the MPM method, the Lagrangian particles contain all the physical quantities, and the Eulerian background cell is adopted to calculate momentum equations and spatial derivatives [17–19].

Moreover, researchers have developed various coupling methods for penetration problems. Ma et al. [20] incorporated the volume of fluid (VOF) and particle-in-cell (PIC) methods, which can effectively solve the two-dimensional problem of dynamic material fracture and failure subjected to the penetration load. Subsequently, Ren et al. [21] improved the particle method which can avoid numerical fluctuations by means of particle mapping transportation within PIC. Attaway et al. [22] coupled smoothed particle hydrodynamics (SPH) method with FEM, in which distinct material regions are discretized with either SPH particles or finite elements with a particle-to-surface contact algorithm used to quantify subsequent material interactions. Drathi [23] presented an element-free Galerkin method to predict upper and lower bounds of the impact resistance of concrete structures. Sherburn [24] introduced a meshfree formulation under the reproducing kernel particle method for modeling the penetration and perforation of concrete, the projectile-slab interaction and the material failure and fragmentation behaviors. Wu [25] proposed and applied a 3D smooth particle Galerkin method to simulate projectile penetration into the concrete slab, obtained the basic response characteristics of concrete to the projectile, and captured the perforation and cratering process of concrete under high-speed impact in the numerical simulation.

The existing methods are rely on improving the Lagrangian or Eulerian methods to simulate projectile penetration into the reinforced concrete slab. The Lagrangian method is traditionally used to solve the penetration problem. Two solutions have been developed to avoid cell distortion in the large deformation: The first one is to re-divide the cell, but the newly generated cell increases the amount of calculation. Secondly, the erosion algorithm relies on the experience of the simulation. The Eulerian method is suitable method for large deformations, such as the penetration problem. However, accurate tracking and dealing with the multi-material interface is required. The coupled methods incorporated and improved the capabilities of current methods, but they cause the numerical fluctuation, insertion between different materials or high computational cost.

Currently, Lagrangian methods work well at multi-material interfaces, but cause issues during large deformations. While the Eulerian method can readily accommodate large deformation, it cannot accurately represent the free surface and multi-material interface. For the numerical simulation of projectile penetration into the reinforced concrete slab, the Eulerian method was utilized to deal with the unpredictable large deformation, while the Lagrangian method was used to precisely track the reinforcing bars in the reinforced concrete. Therefore, considering the limitations of each method, combining the strengths of the Eulerian and Lagrangian methods is required to study the projectile penetration into the reinforced concrete slab.

In this paper, a 3D coupled Eulerian-Lagrangian method is proposed to simulate projectile penetration into the reinforced concrete slab. In this method, for the material which is not required accurately tracking, the material covered with Eulerian cells, such as projectile and concrete target; otherwise, the material covered with both Eulerian cells and Lagrangian particles, such as reinforcing bar. Furthermore, the Lagrangian particles are assumed a certain influence domain, and all the Lagrangian particle influence domains in an Eulerian cell are closely connected and cover the whole Eulerian cell, which can avoid numerical oscillations because of finite particles. The physical quantities of the Eulerian cells and Lagrangian particles are mapped to each other by their topological relationships, which can avoid nonphysical embed between different materials benefit from the single-valued mapping. The MPI standard is adopted to implement large-scale computation. Then, the numerical simulation of projectile penetration into the concrete and reinforced concrete slab are conducted. Numerical simulations of penetration depth, displacement, velocity, and deceleration were compared with the experimental data and those of other published studies. Finally, the deformation history of reinforcing bar during the penetration process, and the influence of initial penetration velocity, reinforcing bar, and the uniaxial compressive strength and thickness of concrete on the penetration performance are conducted. Our results show that the 3D Eulerian-Lagrangian method can effectively and accurately predict projectile penetration into the reinforced concrete slab.

2. Numerical method

Numerical simulation of projectile penetration into the reinforced concrete slab can be challenging due to material large deformation, multi-material interface treatment, parameter variation caused by high pressure and strain rate, strong discontinuity, and new interface formation upon material phase damage or transformation. The material models are based on the continuity assumption to simplify this problem.

2.1. Governing equations

The Euler equations are written in tensor form by neglecting viscosity and heat conduction [26].:

$$\frac{\partial \rho}{\partial t} + \nabla\cdot(\rho \mathbf{u}) = 0 \tag{1}$$

$$\frac{\partial \mathbf{u}}{\partial t} + \mathbf{u}\cdot\nabla\cdot(\mathbf{u}) = \frac{1}{\rho}\nabla\cdot\sigma \tag{2}$$

$$\rho\left(\frac{\partial e}{\partial t} + \mathbf{u}\cdot\nabla\cdot e\right) = \sigma\colon \dot{\varepsilon} \tag{3}$$

where t, $\mathbf{u}$, $\boldsymbol{\sigma}$, $\dot{\varepsilon}$, ρ, and e is the time, velocity, stress tensor, strain rate tensor, density, and specific internal energy, respectively.

The hydro-elasto-plastic model is adopted in this paper [6]. The stress tensor is composed of the hydrostatic pressure and deviatoric stress. The strain is composed of the elastic strain and plastic strain.

$$\sigma_{ij} = -PI_{ij} + S_{ij} \tag{4}$$

$$e_{ij} = e_{ij}^{e} + e_{ij}^{p} = \left(\frac{e_{ii}}{3}\delta_{ij} + \varepsilon_{ij}^{e}\right) + \varepsilon_{ij}^{p} \tag{5}$$

In Eq. (4), PI_{ij} reflects the volume change of the material. The volume change is elastic with no change in shape and can be obtained by the state equation; S_{ij} changes only the shape of the material, reflects the extent of the actual stress state of the material and deviates from the uniform stress state. Numerical simulation of projectile penetration into the reinforced concrete slab involves multiple materials. For the state equations of these materials, the idea gas equation of state, Mie – Grϋneisen equation of state [27] and HJC equation of state [28,29] are used to characterize the material properties of gas, metal and concrete, respectively.

2.2. Operator splitting algorithm

The operator splitting algorithm is adopted [6] to solve the governing equations in this paper. The governing equations are divided into three directions x, y, and z. The conservation equations (Eqs. (1-3)) can be expressed uniformly as:

$$\frac{\partial \varphi}{\partial t} + \mathbf{u}\cdot\nabla\varphi = \mathbf{H} \tag{6}$$

where $\boldsymbol{\varphi}$ represents ρ, e, and $\mathbf{u}$. Therefore, $\mathbf{u}\cdot\nabla\boldsymbol{\varphi}$ and $\mathbf{H}$ are the convection term and source term, respectively. Operator splitting in the sense of physical effects refers to splitting the equation into the following forms:

$$\frac{\partial \varphi}{\partial t} = \mathbf{H} \tag{7}$$

$$\frac{\partial \varphi}{\partial t} + \mathbf{u}\cdot\nabla\varphi = 0 \tag{8}$$

Eqs. (7) and (8) are named the Lagrangian phase and the Eulerian phase, respectively. In the Lagrangian phase, the influence of pressure and deviator stress are considered when calculating the change of velocity and internal energy, and the Eulerian cell is allowed to distort along with the material. In the Eulerian phase, the Eulerian cells deform with the material, and then the redistributed variables of mass, momentum, and energy are calculated using the interface treatment technology.

2.3. HJC concrete model

The HJC model was originally developed for impact computations of concrete where the material experiences high pressure and strain rates [30]. The HJC concrete model is an elastic-viscoplastic model coupled with isotropic damage, where the response is separated into hydrostatic and deviatoric contributions[31]. It should be pointed out that the HJC model uses the elastic-perfectly plastic model to consider the tensile strength of concrete without considering the effects of tensile damage, strain-rate and fracture energy, which has certain limitations for numerical simulation mainly based on tensile phenomena, e.g. cratering and scabbing. Meanwhile, the HJC model was constructed in total stress space without special attention to uniaxial unconfined compression or tension, and the effects of strain-rate and inertia are not distinguished. Therefore, some modified HJC model were proposed by scholars in recent years. Polanco-Lorica et al. [31] proposed three modifications to the HJC model, including the pressure-shear behavior, the strain-rate sensitivity term and the damage description. Liu et al. [32] proposed a modified HJC model, where the dynamic tensile behavior of concrete is described by the TCK model, while the dynamic compressive behavior of concrete is still governed by the HJC model. Islam et al. [33] proposed a modified HJC model by the improved and simplified strain-rate effect term and equation of pressure-volume, which requires smaller number of material parameters. Kong et al. [34] proposed four modifications to the HJC model, including the modified yield surface, introduction of the tensile damage, introduction of Lode-angle dependency and modified strain-rate effect, where the strain-rate effect adopts the semi-empirical equations for DIF of concrete-like materials proposed by Xu et al. [35,36]. Xu et al. [37] developed a computational constitutive model for concrete subjected to dynamic loadings, which takes account of pressure dependency, strain hardening and softening, strain rate effects, Lode effect and failures in both high and low confining pressures, and this model can better predict the sizes of both impact and scabbing craters than the modified K&C model and the modified HJC model.

A credible and accurate materials model can more accurately describe the material behavior of concrete under different loading conditions. However, the theoretical basis of the HJC model is relatively simple and considers most of the important issues of concrete behavior. Thus, the HJC model is widely used for impact problems because of its relatively small number of material parameter requirements. Refs. [38–44] also demonstrate the HJC model is a simple, effective and accurate model for penetration studies. This concluded that the HJC concrete model offers favorable trade-off between simplicity and accuracy for large-scale computations. Therefore, the HJC model [30] is adopted in this paper.

In this paper, the normalized equivalent stress [31] can be expressed by the constitutive relation

$$\sigma^* = [A(1-D) + BP^{*N}](1 + C\ln\dot{\varepsilon}^*) \tag{9}$$

where $\sigma^* = \sigma/f_c$ is the normalized equivalent stress; $\sigma = \sqrt{\frac{3}{2}S_{ij}S_{ij}}$ is the von Mises equivalent stress, in which S_{ij} is the stress deviator; f_c is the static uniaxial compressive strength of concrete; D is the damage variable, resulting in reduction of the cohesive strength. In a complete damaged state with $D = 1$, the concrete behaves as a granular material characterized by a certain residual strength envelop [31]; $P^* = P/f_c$ is the normalized pressure; $\dot{\varepsilon}^* = \dot{\varepsilon}/\dot{\varepsilon}_0$ is the normalized strain rate, where $\dot{\varepsilon}_0$ is the reference strain rate; A, B, N, and C are the material constant, they respectively represent the cohesion strength, pressure hardening, pressure hardening exponent and strain-rate sensitivity coefficient. Due to the lack of test data, Holmquist et al. [30] assumed that the cohesive strength A as $0.75f_c$ for quasi-static conditions ($\dot{\varepsilon} = 0.001$) and determined $A = 0.79$ by normalizing to $\dot{\varepsilon} = 1.0$. The B and N are determined by fitting the triaxial compression test data without considering the influences of damage and strain-rate. The strain-rate coefficient C is determined by the fitting the different uniaxial compression test data of removing the pressure effect.

The HJC concrete model describes compression damage through the equivalent plastic strain increment and the plastic volumetric strain increment, and its evolution equation [30] is expressed as

$$D = \sum \frac{\Delta\varepsilon_p + \Delta\mu_p}{D_1(P^* + T^*)^{D_2}} \tag{10}$$

where $\Delta\varepsilon_p$ and $\Delta\mu_p$ are equivalent plastic strain and plastic volume strain, D_1 and D_2 are material damage constants. The damage parameters are usually determined by a cylinder specimen subjected to cyclic compression loadings. Due to the limited available test data, the original damage parameters $D_1 = 0.04$ and $D_2 = 1.0$ referring to Ref. [30]. $T^* = T/f_c$ is normalized maximum tensile hydrostatic pressure, where T is maximum tensile hydrostatic pressure, which is determined by the specific test data. If the related test data are missing, E and T are simply determined by the equations $E = 0.043\rho_0^{3/2}f_c^{1/2}$ and $T = 0.62f_c^{1/2}$ referring to Ref. [45].

The HJC concrete model uses the three-stage state equations to describe the relationship between hydrostatic pressure and volume strain of concrete, which can be divided into the linear elastic, plastic transition and compacted stages [30].

In the loading stage

$$P = \begin{cases} \mu K_{elastic} & P < P_{crush} \\ & \text{linear elastic stage} \\ P_{crush} + \dfrac{P_{lock} - P_{crush}}{\mu_{plock} - \mu_{crush}}(\mu - \mu_{crush}) & P_{crush} \le P \le P_{lock} \\ & \text{plastic transition stage} \\ K_1\overline{\mu} + K_2\overline{\mu}^2 + K_3\overline{\mu}^3 & P > P_{lock} \\ & \text{compacted stage} \end{cases} \tag{11}$$

where

$$\overline{\mu} = \frac{\mu - \mu_{lock}}{1 + \mu_{lock}}, \quad \mu = \frac{\rho}{\rho_0} - 1 \tag{12}$$

In the unloading stage

$$P = \begin{cases} \mu K_{elastic} & \text{linear elastic stage} \\ [(1-F)K_{elastic} + FK_1]\mu & \text{plastic transition stage} \\ K_1\mu & \text{compacted stage} \end{cases} \tag{13}$$

where

$$F = \frac{\mu_{max} - \mu_{crush}}{\mu_{lock} - \mu_{crush}} \tag{14}$$

where P is the hydrostatic pressure, and μ represents the volumetric strain; P_{crush} and μ_{crush} are the critical pressure and the volumetric strain when the gap in the material begins to close, respectively; P_{lock} is the critical pressure when the material gap is totally closed; $K_{elastic}$ is the elastic bulk modulus; μ_{lock} is the volumetric strain under P_{lock}. $T(1-D)$ is the stretching pressure limit; T is the tensile strength; D is the damage degree of concrete. K_1, K_2 and K_3, which are represented the concrete in the full crushed state, are determined based on the Hugoniot data for granite and quartz, and the locking pressure P_{crush} is determined by fitting the test data.

2.4. Multi-material interface treatment technology

In the Eulerian phase, the core is the multi-material interface processing technology, which determines the sharpness of the interface between different materials. Currently, the volume-of-fluid (VOF) methods [46], piecewise linear interface construction (PLIC) methods [47] and level-set methods [48] are the typical interface treatment methods for multi-material interfaces. However, these methods are difficult to deal with multi-material in 3D problems.

In this study, we adopted the fuzzy interface treatment method [26] for the 3D multi-material interface treatment. In this method, the volume ratio of the material is used as the fuzzy weight coefficient, which determines the transport of physical quantities between Eulerian cells. Meanwhile, according to the priority in the weight of the transported materials, the transport order can be formulated. Fuzzy interface treatment can easily arrange mixture cells involving three or more materials in three-dimensional regions with lower computational cost compared to other interface treatment methods.

3. 3D coupled Eulerian-Lagrangian method

The 3D coupled Eulerian-Lagrangian method is proposed to accurately track the deformation history of reinforcing bar during projectile penetration into the reinforced concrete slab. In the 3D coupled Eulerian-Lagrangian method, the Lagrangian particles are assumed a certain influence domain, and all the Lagrangian particle influence domains in a Eulerian cell are closely connected, covering the whole Eulerian cell; thus, the technique avoids numerical oscillations due to finite particles. The physical quantities of the Eulerian cell and Lagrangian particles are mapped to each other by their topological relationships to avoid nonphysical embed between different materials benefit from the single-valued mapping.

3.1. Implementation process

The 3D coupled Eulerian-Lagrangian method consists of the following four steps:

Step 1: Lagrangian particle initialization

The Lagrangian particles are added to the Eulerian cells to track the deformation of the reinforcing bars. The distribution principle is that all the Lagrangian particle influence domains in an Eulerian cell are closely connected and cover the whole Eulerian cell. In this study, the equidistant distribution is adopted, as shown in Fig. 1.

Lagrange particles η which is an integer and it's greater than or equal to 2 are arranged in each direction, thus, the total number of Lagrangian particles in an Eulerian cell is $K = \eta^3$. $\Delta\mathbf{L}_P = [\Delta L_{px}, \Delta L_{py}, \Delta L_{pz}]^T$ and $\Delta\mathbf{X}_E = [\Delta x_E, \Delta y_E, \Delta z_E]^T$ are defined as the step of the influence domain of Lagrangian particle and Eulerian cell, respectively, where ΔL_{px}, ΔL_{py}, ΔL_{pz} and Δx_E, Δy_E, Δz_E are the corresponding step in each direction. Thus, $\Delta\mathbf{L}_P$ can be obtained by Eq. (15).

$$\Delta\mathbf{L}_P = \frac{1}{\eta}\Delta\mathbf{X}_E \tag{15}$$

$\mathbf{L}_P = [L_{px}, L_{py}, L_{pz}]^T$ and $\mathbf{X}_E = [x_E(i), y_E(j), z_E(k)]^T$ are defined as the Lagrangian particle coordinate and Eulerian cell coordinates, respectively, where the L_{px}, L_{py}, L_{pz} and $x_E(i)$, $y_E(j)$, $z_E(k)$ are the corresponding central coordinate in the direction of x, y and z, respectively. The $\mathbf{I} = [I_1, I_2, I_3]^T$ is defined as the location index of the Lagrangian particle in an Eulerian cell, it's value relate to the distribution and η. For the scenario in this paper, $I_i = 2\delta - 1, \quad i \in [1, 3]$, where the value of δ is an integer of $[1, \eta]$. The initial location coordinates of the Lagrangian particle can be obtained from Eq. (16):

$$\mathbf{L}_P = \mathbf{X}_E - \frac{1}{2}\Delta\mathbf{X}_E + \frac{1}{2\eta}\mathbf{I}\cdot\Delta\mathbf{X}_E \tag{16}$$

Then, the initialization physical quantities of the Lagrangian particle can be obtained by the following equation:

$$\begin{bmatrix} \rho_p \\ m_p \end{bmatrix} = \begin{bmatrix} \rho_0 \\ \rho_p \cdot V_p \end{bmatrix} \tag{17}$$

where ρ_p and ρ_0 are the density of Lagrangian particle and Eulerian cell, respectively; m_p is the mass of Lagrangian particle; $V_p = \Delta L_{px} \times \Delta L_{py} \times \Delta L_{pz}$ is the influence domain volume of Lagrangian particle.

Step 2: Mapping physical quantities of Eulerian cells to Lagrangian particles

Before each step loop, it is necessary to map the physical quantity of the Eulerian cell to the Lagrangian particles based on the topological relationship between the Eulerian cell and the particle influence domain. The topological relationship between the Lagrangian particles influence domain and the Eulerian cell can be divided into 4 classes according to the positional relationship between them, as shown in Fig. 2, for a total of 27 relationships. Table 1 shows the specific classified information of the four classes.

Fig. 2 and Table 1 show that the most complex scenario for the topological relationship is for class 4, where the Lagrangian particles influence domain overlaps with 8 adjacent Eulerian cells. The overlapping volumes between the influence domain of a Lagrangian particle and 8 adjacent Eulerian cells are defined as V_f, where $f \in [1, 8]$.

For class 4, the overlapping volumes can be calculated as follows:

The index number of overlapping volumes in the adjacent Eulerian cells is shown in Table 2. If $\mathbf{L}_P > \mathbf{X}_E$, the Eulerian cell index number adopt +; otherwise, the Eulerian cell index number adopt −.

The V_f can be obtained:

$$V_f = \left| \begin{array}{l} \left[L_{px} + \alpha\cdot l\cdot\frac{1}{2}\Delta L_{px} - \left(x_E(i) + l\cdot\frac{1}{2}\Delta x_E \right) \right] \\ \cdot \left[L_{py} + \beta\cdot m\cdot\frac{1}{2}\Delta L_{py} - \left(y_E(j) + m\cdot\frac{1}{2}\Delta y_E \right) \right] \\ \cdot \left[L_{pz} + \gamma\cdot n\cdot\frac{1}{2}\Delta L_{pz} - \left(z_E(k) + n\cdot\frac{1}{2}\Delta z_E \right) \right] \end{array} \right| \tag{18}$$

where α, β, γ, l, m, and n are constant coefficients, and their values are -1 or 1. Table 3 gives the values of α, β, and γ in 8 adjacent Eulerian cells. The values of l, m, and n can be calculated according to the topological relationship between the Lagrangian particle and it located Eulerian cell. If $L_{px} > x_E$, $l = 1$; otherwise, $l = -1$; If $L_{py} > y_E$, $m = 1$; otherwise, $m = -1$; If $L_{pz} > z_E$, $n = 1$; otherwise, $n = -1$.

The overlapping volumes for classes 1, 2 and 3 can be calculated by simplified class 4. For the scenario of class 1, as shown in Fig. 2(a), only V_1 has a value, and the rest are both equal to 0. V_1 can be calculated by Eq. (19):

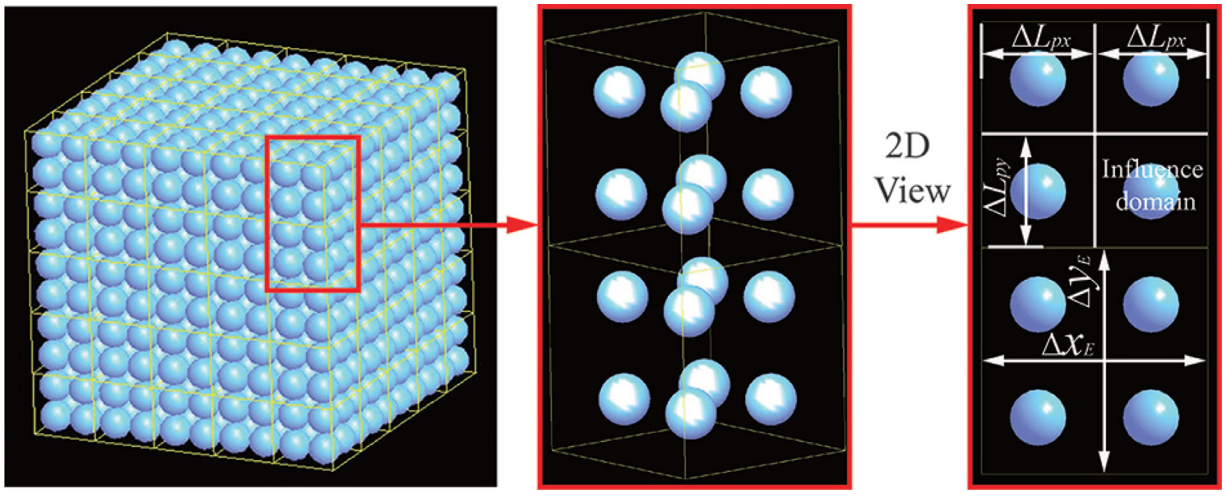

Fig. 1. Distribution of Lagrangian particles in Eulerian cells.

$$V_1 = |\Delta L_{px} \cdot \Delta L_{py} \cdot \Delta L_{pz}| \tag{19}$$

For the scenario of class 2, as shown in Fig. 2(b), only V_1 and V_5 have values, which can be calculated by Eq. (20):

$$V_f = \left| \left[L_{px} + \alpha \cdot l \cdot \frac{1}{2}\Delta L_{px} - \left(x_E(i) + l \cdot \frac{1}{2}\Delta x_E \right) \right] \cdot \Delta L_{py} \cdot \Delta L_{pz} \right| \tag{20}$$

For the scenario of class 3, as shown in Fig. 2(c), only V_1, V_2, V_5 and V_6 have values, which can be calculated by Eq. (21):

$$V_f = \left| \begin{array}{l} \left[L_{px} + \alpha \cdot l \cdot \frac{1}{2}\Delta L_{px} - \left(x_E(i) + l \cdot \frac{1}{2}\Delta x_E \right) \right] \cdot \Delta L_{py} \\ \cdot \left[L_{pz} + \gamma \cdot n \cdot \frac{1}{2}\Delta L_{pz} - \left(z_E(k) + n \cdot \frac{1}{2}\Delta z_E \right) \right] \end{array} \right| \tag{21}$$

The influence domains of all Lagrangian particles in the Eulerian cell with the statistical cell index number D are combined and expressed as $\sum_{s=1}^{N} V_{Ds}$. $\mathbf{Q}_P$ and $\mathbf{Q}_E$ are defined as the physical quantities of Lagrangian particle and Eulerian cell, respectively. Based on the topological relationship as shown in Fig. 2, $\mathbf{Q}_E$ can be mapped to $\mathbf{Q}_P$ by overlapping volumes, the specific equation is shown as follow:

$$\mathbf{Q}_p = \sum_{f=1}^{8} \frac{V_f}{\sum_{s=1}^{N} V_{Ds}} \mathbf{Q}_{Ef} \tag{22}$$

Step 3: Lagrangian particle movement

The $\mathbf{u}_p = [u_p, v_p, w_p]^{\mathrm{T}}$ and $\mathbf{u}_E = [u_E, v_E, w_E]^{\mathrm{T}}$ are defined as the Lagrangian particle velocity and Eulerian cell velocity, respectively. The $\mathbf{u}_p$ can be obtained by the volume weighting Eq. (23).

Table 1
Specific classified information of the four classes .

Classification number	Cutting position of Eulerian cell	Weighted Eulerian cells number	Types of topological relationship
Class 1	-	1	1
Class 2	face	2	6
Class 3	edge	4	12
Class 4	vertice	8	8

Table 2
Eulerian cell index number of each overlapping volume .

Number of f	Index Eulerian cell number
1	(i, j, k)
2	$(i \pm 1, j, k)$
3	$(i \pm 1, j \pm 1, k)$
4	$(i, j \pm 1, k)$
5	$(i, j, k \pm 1)$
6	$(i \pm 1, j, k \pm 1)$
7	$(i, j \pm 1, k \pm 1)$
8	$(i \pm 1, j \pm 1, k \pm 1)$

$$\mathbf{u}_p = \sum_{f=1}^{8} \frac{V_f}{V_p} \mathbf{u}_E \tag{23}$$

Then, the Lagrangian particle coordinates at the next time step are given by

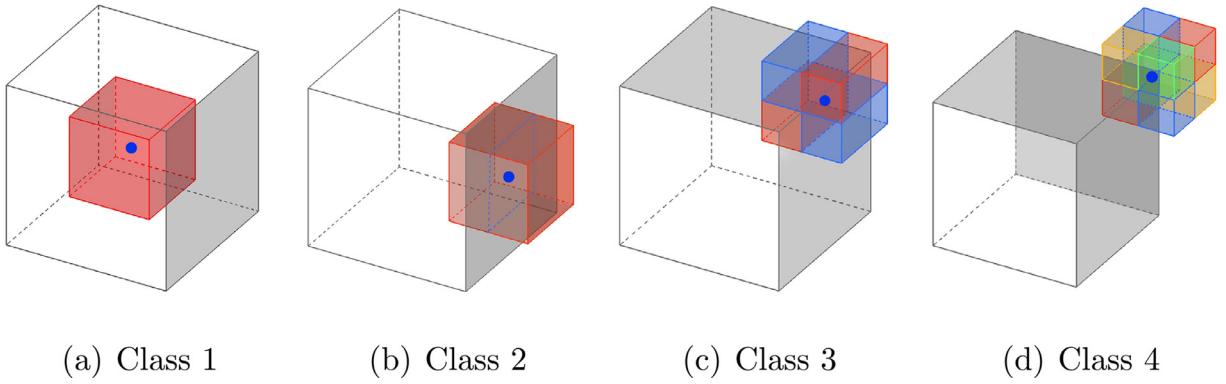

Fig. 2. Lagrangian particles influence domain located in the domain of Eulerian cell.

Table 3
The values α, β, and γ of 8 adjacent Eulerian cells .

	V_1	V_2	V_3	V_4	V_5	V_6	V_7	V_8
α	-1	1	-1	1	-1	1	-1	1
β	-1	-1	1	1	-1	-1	1	1
γ	-1	-1	-1	-1	1	1	1	1

$$\mathbf{X}_E^{n+1} = \mathbf{X}_E^{n} + \mathbf{u}_p \cdot \Delta t \tag{24}$$

Step 4: Physical quantities of Lagrangian particles map to the Eulerian cells

After each time step, the position of the Lagrangian particle and the topological relationship between the Lagrangian particle and the Eulerian cell change. The new V_f can be obtained as the step 2.

Thus, the number of Lagrangian particles with influence domains in the Eulerian cell is added to the statistical cell index number D and record the index number of Lagrangian particles. The total number and the index number of Lagrangian particles are N_D and n_D. The $V_{n \to D}$ is defined as the overlapping volume of Lagrangian particle n_D in the Eulerian cell D. Thus, the physical quantity of Lagrangian particle n_D contributes to the Eulerian cell D can be obtained by the Eq. (25).

$$\mathbf{Q}_{Dn} = \frac{V_{n \to D}}{V_p} \mathbf{Q}_P \tag{25}$$

The physical quantities of the cell D can be obtained by summing the N_D Lagrangian particles:

$$\mathbf{Q}_D = \sum_{n=1}^{N_D} \frac{V_{n \to D}}{V_p} \mathbf{Q}_p \tag{26}$$

After the above steps, the physical quantities of the Eulerian cell transported between cells are performed by the movement of the Lagrangian particles.

3.2. Parallelization of the 3D coupled eulerian-Lagrangian method

The 3D coupled Eulerian-Lagrangian method adopts Lagrangian particles to simulate material flow in Eulerian cells. The Lagrangian particle movement modifies the physical quantities of the adjacent Eulerian cell due to the topological relationship between Lagrangian particles and Eulerian cells. When a Lagrangian particle moves to a process boundary, it requires communication between the processes, and sends the physical quantities carried by the Lagrangian particle from one process to another.

There were two types of variables in the program, one of which was shared by all processes on the system, and the other one was private in a single process. The shared variables are the same for all processes, while the private variables may have different values in different processes. All the shared variables should be broadcast to all processes; however, only the private variables on the boundaries should be sent to adjacent processes after updating.

In this study, we use private variables and shared variables communication mode, as shown in Fig. 3. The private variables include process ID, Eulerian cell ID, Lagrangian particle ID, and physical variables such as pressure,density, velocity,mass, and volume. The shared

Table 4
HJC model parameters with a compressive strength of 23.0 MPa [51] .

Density (g/cm^3)	2.04	S_{max}	30.0
Shear modulus (GPa)	7.917	P_{crush} (GPa)	0.007667
A	0.79	μ_{crush}	0.00128
B	1.3871	P_{lock} (GPa)	0.596
C	0.007	μ_{lock}	0.299
N	0.37625	D_1	0.036
f_c (MPa)	23.0	D_2	1.0
T (MPa)	2.55	K_1 (GPa)	85
EFMIN	0.01	K_2 (GPa)	-171
$\dot{\varepsilon}_0$	1×10^{-6}	K_3 (GPa)	208

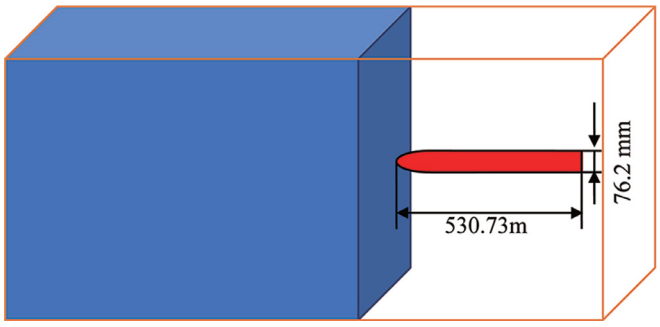

Fig. 4. The geometry and calculation model of projectile.

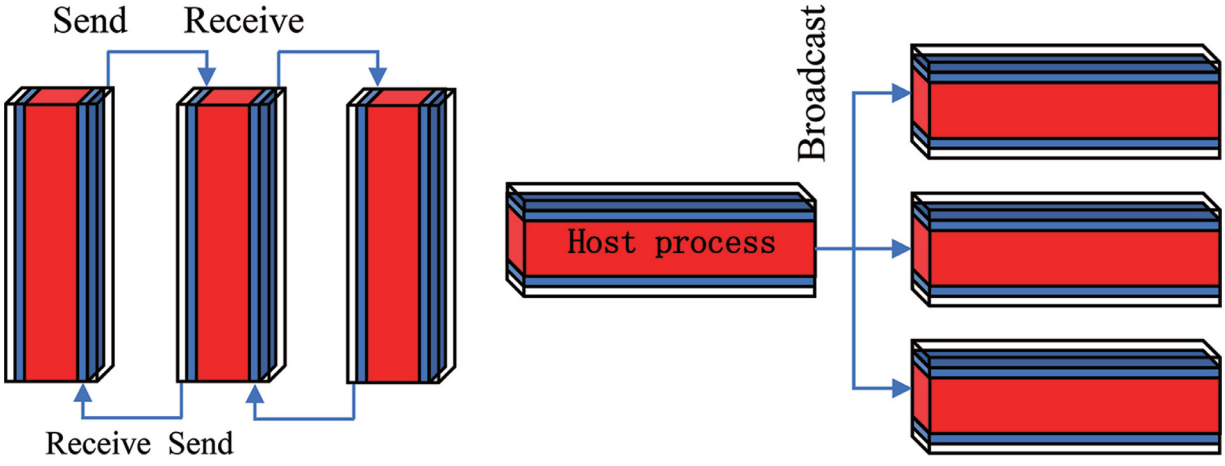

(a) Private variable communication (b) Shared variable communication

Fig. 3. Communication diagram of two variables.

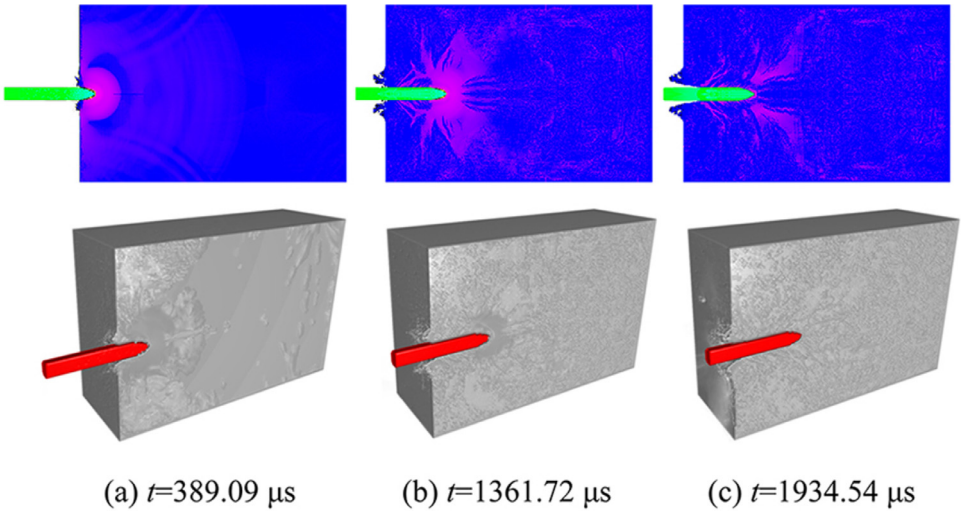

Fig. 5. Projectile penetration into the concrete slab with an initial impact velocity of 200.0 m/s.

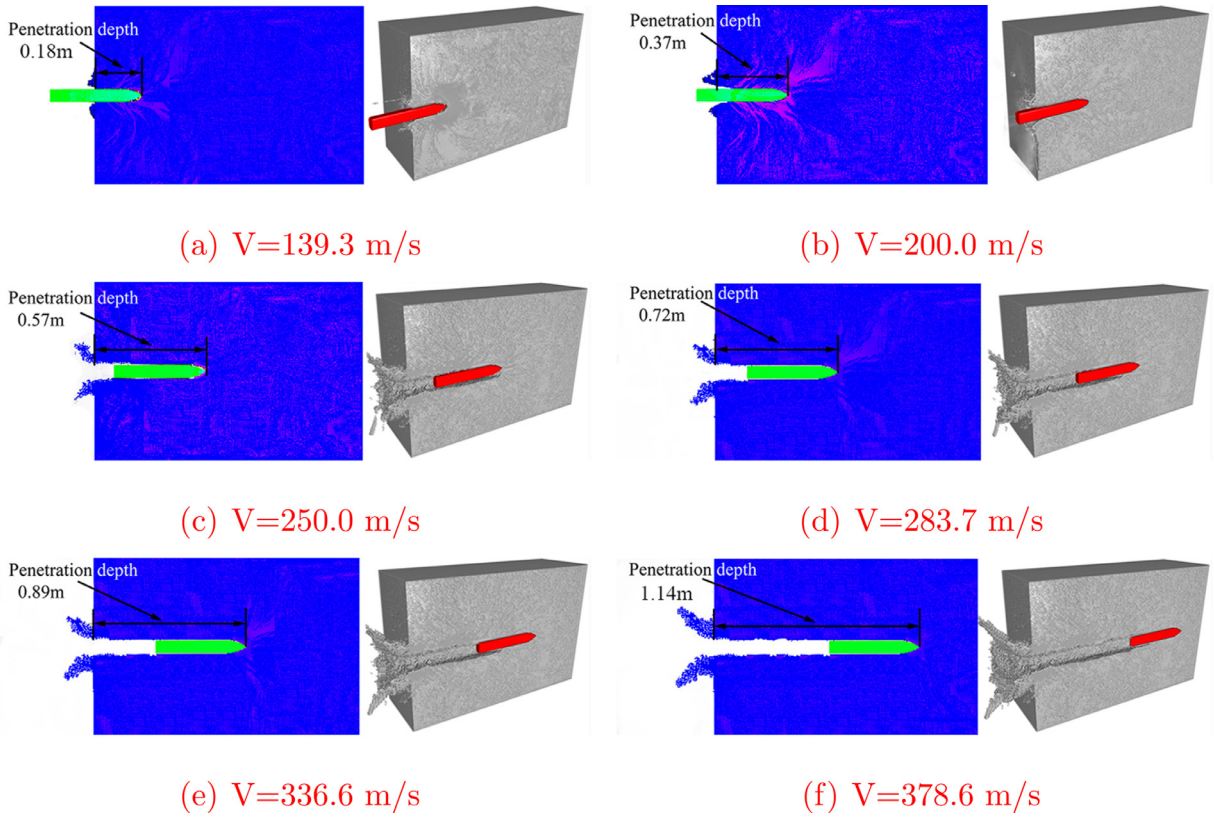

Fig. 6. Numerical results of the projectile penetration into concrete with different initial impact velocities.

variables include total mass, total volume, total momentum of the material, the position of the target, and the parameters of the EOS (equation of state).

4. Numerical simulation of projectile penetration into the concrete slab

In this section, all numerical examples are conducted by a four-node cluster. Each node had two Intel E5620 CPUs; the memory is 32 G, and every CPU get six cores in it. Experiment of ogive-nosed projectile normal penetration into concrete slab was reported by Forrestal [49,50].

4.1. Calculation model

The ogive-nosed projectile geometric parameters are m = 13.0 kg, d = 76.2 mm, CRH = 3.0, and projectile material is 4340Rc45 steel. The size of the concrete slab is 100cm × 100cm × 150cm, and the average compressive strength is 23.0 MPa with a stander deviation of 2.4 MPa [50]. The material parameters of the HJC model for 23.0 MPa concrete in Ref. [51] are adopted, and the specific parameters are shown in Table 4. The geometry and calculation model of the projectile is shown in Fig. 4. The projectile hardly deforms during penetration due to the low impact velocity. Therefore, the projectile is treated as rigid and does not deform during the penetration process in the numerical simulation. The computational domain is 100 cm × 100 cm × 200 cm.

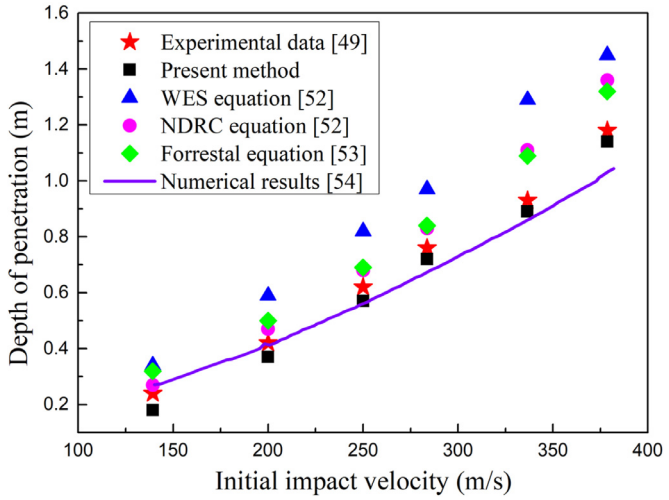

Fig. 7. Comparison of the present method with the empirical equations, previous numerical results [54]and experimental data [49] for depth of penetration versus initial impact velocity.

The Eulerian cell step size is 4 mm, and totaling 31.25 million Eulerian cells. The calculated time are 6 h, 9 h, 12 h, 14 h, 17 h, and 21 h for initial impact velocity of 139.3 m/s, 200.0 m/s, 250.0 m/s, 283.7 m/s, 336.6 m/s, and 378.6 m/s, respectively. The projectile penetration into the concrete slab with 31.25 million Eulerian cells took less than a day, indicating that the proposed numerical method is very efficient.

4.2. Numerical results

Fig. 5 shows the projectile penetration into the concrete slab with an initial impact velocity of 200.0 m/s. When the projectile impacts the concrete slab, the high pressure is formed on the part of the concrete surface, as shown in Fig. 5 (red area in the 2D graph). The high pressure damages concrete, and forms the crushed zone. Then, the stress wave energy attenuates with propagating outwards, and form the plastic zone outside the crushed zone. When the stress amplitude is lower than the stress of the elasticity limit of the concrete, the stress waveforms the elastic zone. The fragments on the concrete and projectile interface apparently flow with the penetration, and it forms a tunnel area in the concrete. The numerical simulation is in good agreement with the actual physical phenomena. Fig. 6 shows the final 2D and 3D numerical results of projectile penetration into concrete slabs with different initial impact velocities.

4.3. Comparison of numerical results with the experimental data

The validation and capability of the numerical method are shown in Fig. 7, with the results of empirical equations. The numerical results are lower than those of experimental data, while the errors are smaller with increased initial impact velocity. The results of WES (US. Waterway Experiment Station) equation [52] are higher compared with the experimental data, and the errors are increase with the initial impact velocity increasing. The results of NDRC (US. National Defense Research Committee) equation [52] are close to that of the Forrestal's equation [53]. Their predictions at low initial velocities were consistent with the experimental data, but the errors increase with impact velocity. Furthermore, in Fig. 7, we compare the depth of penetration obtained from the present method, experimental data in Ref. [49], and the numerical results in Ref. [40]. The results show that the numerical simulation results obtained by the present method are in good agreement with the experimental data. In all cases, the depth of penetration is both slightly underpredicted by the present method and the numerical method in Ref. [54]. When the initial impact velocity is lower than 250.0 m/s, the differences between the present method and the previous numerical method in Ref. [54] with the experimental data [49] are the similar. However, with the increase of initial impact velocity, the results predicted by the present method are closer to the experimental data [49] than those predicted by the numerical method in Ref. [54].

In Fig. 8, we compare the deceleration records obtained from the present method, experimental data [49], the model predicted in Ref. [49], and the numerical results in Ref. [54] with initial velocities of 139.3 m/s, 200.0 m/s, 250.0 m/s, 336.6 m/s and 378.6 m/s. The comparison results show that the numerical simulation results by the present method are consistent with the experimental data. In all cases, the penetration duration values are slightly underestimated, and the amplitude of deceleration values are slightly overestimated by the present method and the numerical method in Ref. [54]. However, in the ascent stage of deceleration, the results predicted by the present method are closer to the experimental data than those of the numerical method in Ref. [54] and the model in Ref. [49]. The penetration duration predicted by the present method is longer than that predicted by the numerical method in Ref. [54], except for the initial impact velocity of 139.3 m/s, but slightly shorter than that predicted by the model Ref. [49]. The amplitude of deceleration predicted by the present method is lower than that predicted by the numerical method in Ref. [54] and more consistent with the experimental data with the increase of initial impact velocity.

Fig. 9 shows the impact velocity and displacement versus time at different initial impact velocities. We compare the impact velocity and displacement records obtained from the present method and the experimental data [49] at an initial impact velocity of 250.0 m/s. The impact velocity and displacement are in good agreement with the experimental data before 2.0 ms. After that, the decrease rate of impact velocity is slightly higher, whereas the increase rate of displacement is lower the experimental data. The comparison of different initial impact velocities shows that the impact velocity decrease and displacement increase are approximately linear at the beginning of the penetration. As the penetration continues, the decrease rate of impact velocity and the increase rate of displacement decrease.

5. Numerical simulations of projectile perforation of reinforced concrete slabs

In this section, all numerical examples are conducted by a eight-node cluster. The performance of each node is the same as in Section 4. The numerical simulation results are compared with the high-speed photograph of the projectile perforation of the reinforced concrete and the slab damage process to verify the validity of the numerical method. Then, the effects of initial impact velocity, reinforcing bar, and the uniaxial compressive strength and thickness of concrete on perforation performance are discussed.

The comparative experiment from Ref. [4] was carried out. The ogive-nosed projectile assume as rigid in the simulation, and its geometric parameters are $m = 9.7$ kg, $d = 100$ mm, CRH = 1.2, respectively, as shown in Fig. 10(a). The reinforced concrete slabs designed for this experiment are shown in Fig. 10(b). In this simulation, the slab model was the same as in the experiment. The average compressive strength is 50.0 MPa with a standard deviation of 3.0 MPa [4], which is basically consistent with the 48.0 MPa concrete. Thus, the material parameters of the HJC model for 48.0 MPa concrete in Ref. [30] are adopted, and the specific parameters are shown in Table 5. The reinforcing bars are described by the Mie – Grÿneisen state equation which is widely used in the dynamic behavior of metal materials under high pressure and strain rate. The expression is as follow:

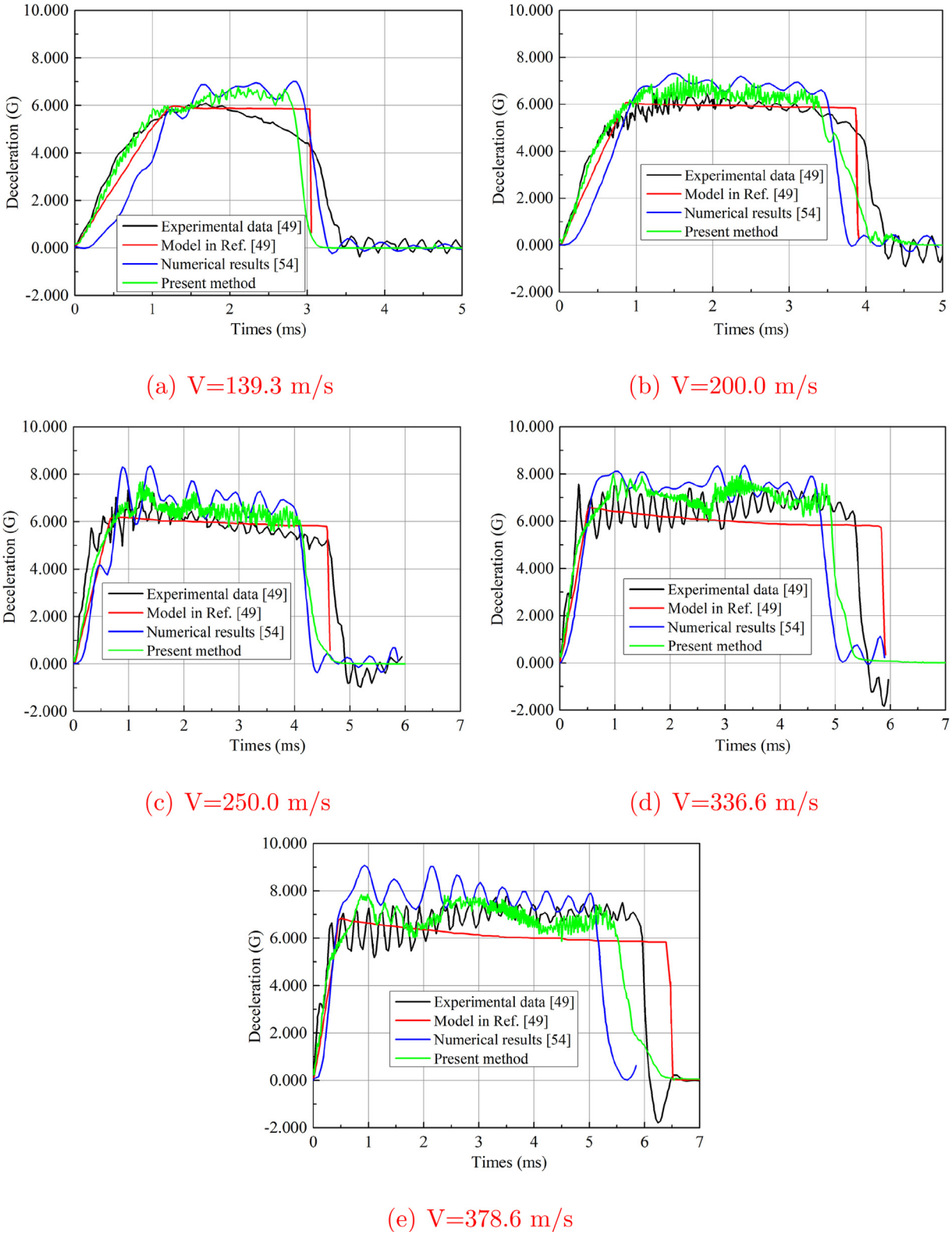

Fig. 8. Comparison of the present method with previous numerical results [54] and experimental data [49] for deceleration versus time .

$$P = \begin{cases} \dfrac{\rho_0 c_0^2 \mu \left[1 + \left(1 - \frac{\gamma_0}{2}\right)\mu - \frac{a}{2}\mu^2\right]}{\left[1 - (s_1 - 1)\mu - s_2 \frac{\mu^2}{\mu+1} - s_3 \frac{\mu^3}{\mu+1}\right]} + (\gamma_0 + a\mu)e, & \mu \geq 0 \\ \rho_0 c_0^2 \mu + (\gamma_0 + a\mu)e, & \mu < 0 \end{cases} \tag{27}$$

where where P is the hydrostatic pressure; a is the Grüneisen gamma, and a is the first order volume correction to γ_0; $\mu = \rho/\rho_0 - 1$, in which ρ_0 and ρ are the initial and local densities, respectively; c_0 is sound velocity; e is the local specific internal energy; constant s_1, s_2, s_3 are the fitting coefficients of relationship on the particle velocity and the shock wave velocity. The material parameters are shown in Table 6.

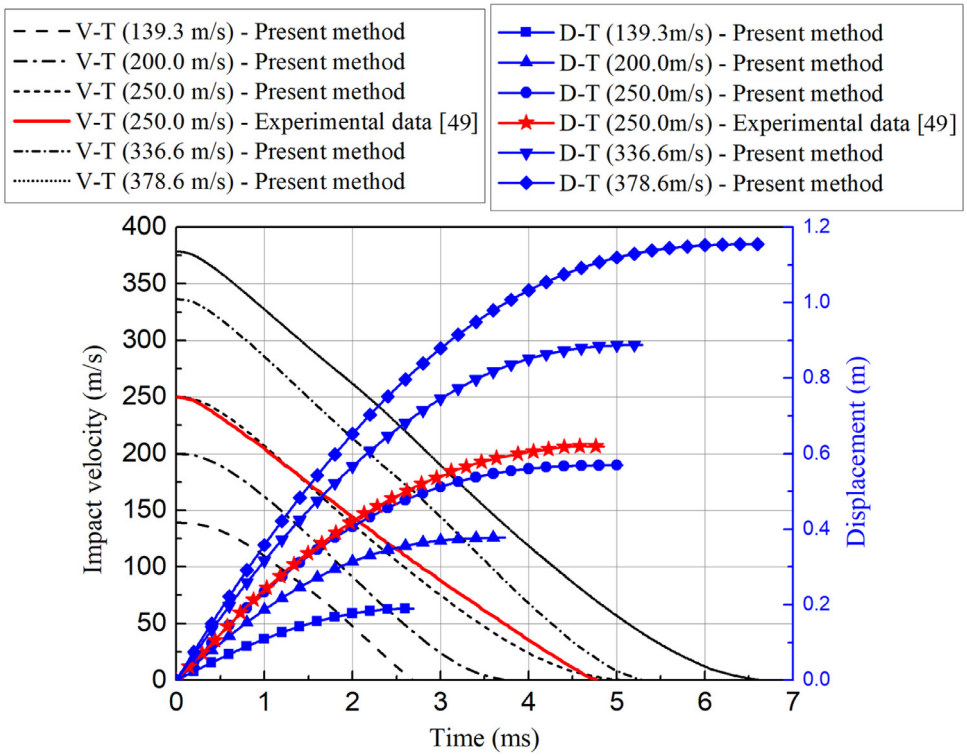

Fig. 9. Comparison of the present method with experimental data [49] for impact velocity and displacement versus time.

(a) Experimental projectile (b) Layout of the reinforcing bars

Fig. 10. Projectile and reinforcing bars layout of the experiment [4].

Table 5
HJC model parameters with a compressive strength of 48.0 MPa [30] .

Density (g/cm^3)	2.44	S_{max}	7.0
Shear modulus (GPa)	14.86	P_{crush} (GPa)	0.016
A	0.79	μ_{crush}	0.001
B	1.6	P_{lock} (GPa)	0.8
C	0.007	μ_{lock}	0.1
N	0.61	D_1	0.04
f_c (MPa)	48.0	D_2	1.0
T (MPa)	4.0	K_1 (GPa)	85
EFMIN	0.01	K_2 (GPa)	-171
$\dot{\varepsilon}_0$	1×10^{-6}	K_3 (GPa)	208

Table 6
Mie – Grüneisen state equation parameters of reinforcing bars.

Density (g/cm^3)	c_0	r	a	s_1	s_2	s_3
7.86	4600	2.0	0.43	1.33	0.0	0.0

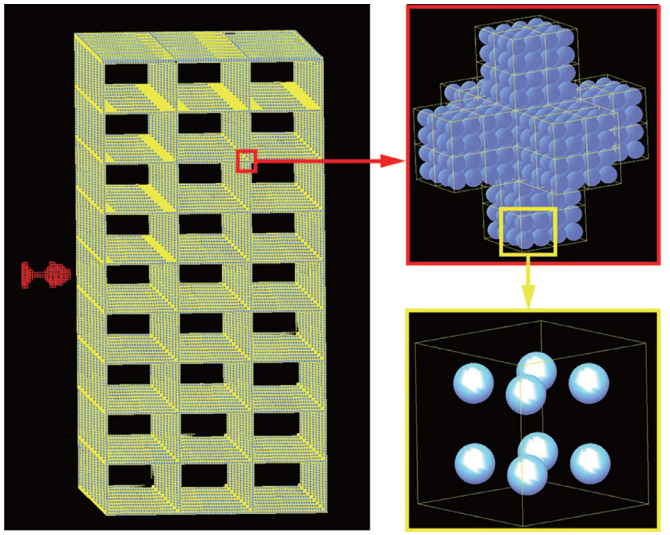

Fig. 11. Computational model of the projectile perforation of the reinforced concrete slab.

5.1. Comparison of numerical results and experimental data

The pre-processing software PMESH-3D [55] which can quickly generate Eulerian cells for complex large-scale problems is adopted to conduct the mesh model. The computational model of the projectile perforation of the reinforced concrete slab is shown in Fig. 11. The

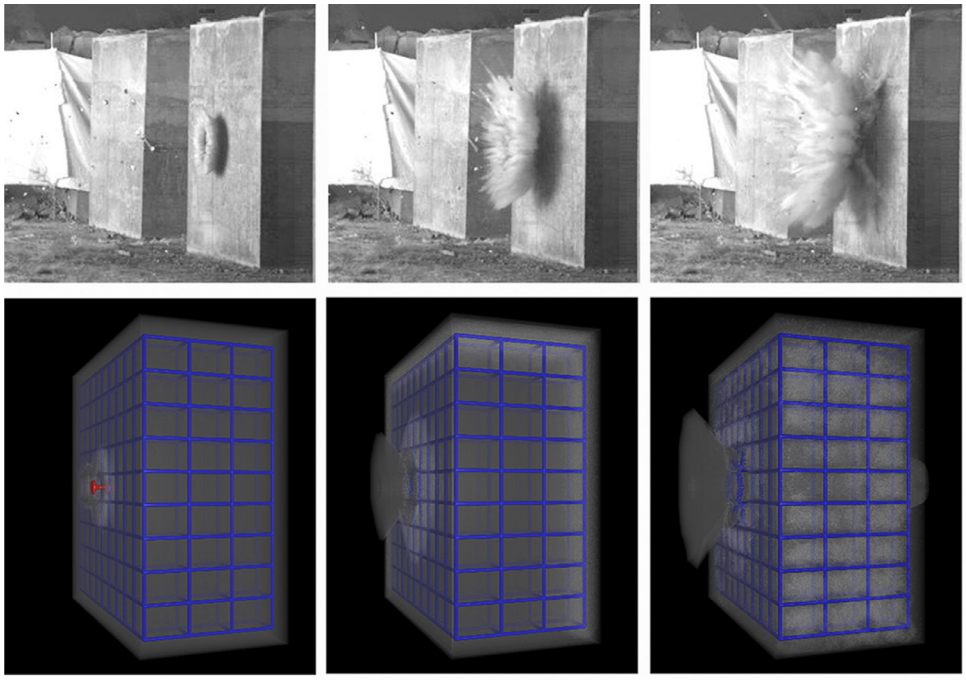

(a) The front face of reinforced concrete slab

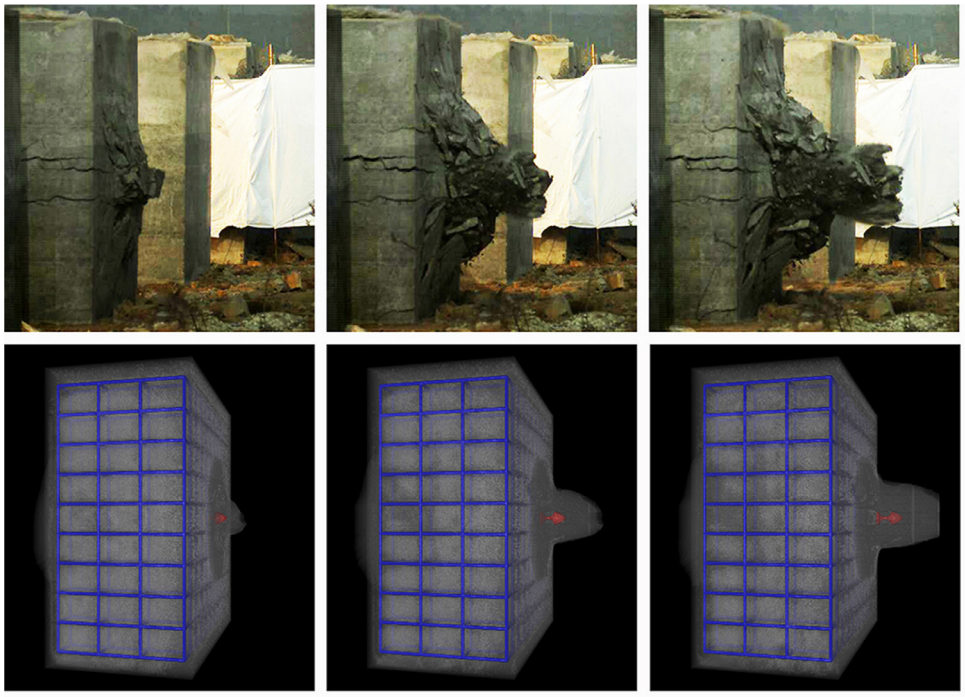

(b) The back face of reinforced concrete slab

Fig. 12. Comparison of numerical and experimental results of the penetration of the reinforced concrete slab.

concrete material does not display to observe better the distribution of reinforcing bars inside the slab. The size of the calculation domain is 2400 mm × 2400 mm × 1800 mm. The Eulerian cell step size is 3.0 mm, totaling 384.0 million Eulerian cells. For the Eulerian cell with the reinforcing bar uniform distributed 64 Lagrangian particles, totaling 14.25 million Lagrangian particles. For this scenario, the computation time is 210 hours. For the projectile penetration into the reinforced concrete slab problem with 384.0 million Eulerian cells and 14.25 million Lagrangian particles, completing numerical calculations take less than 10 days, indicating that the proposed numerical method is very efficient. Because the developed program can complete the numerical calculation of hundreds of millions of Euler cells and tens of millions of Lagrangian particles, it can be applied to the calculation of more complex and large-scale practical engineering problems.

The numerical and experimental results of the reinforced concrete penetration are shown in Fig. 12. The front and back of the target have

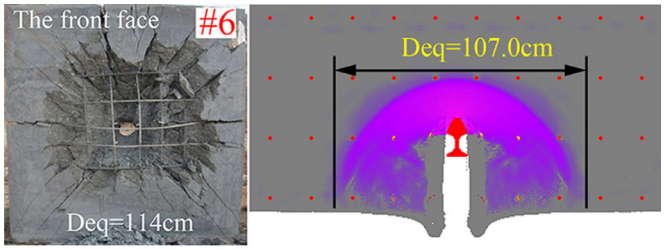

(a) The front face damage of reinforced concrete slab

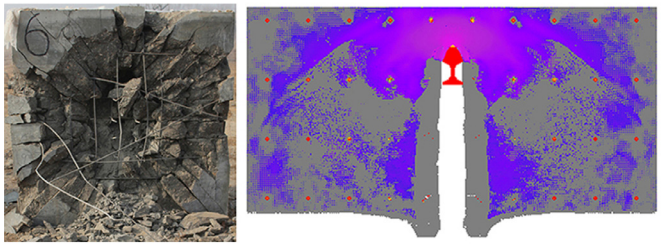

(b) The back face damage of reinforced concrete slab

Fig. 13. Comparison of numerical results and experimental results of reinforced concrete slab failure.

fewer concrete fragments in the numerical simulation than those in the experiments. The main reasons for this error are as follows: (1) the continuity hypothesis in the numerical simulation. The conservative estimation is adopted to keep the code running, and it restricts the concrete material, without free motion that exists in the experiments. The material models are based on the continuity assumption, which leads to a discrepancy with the test results. In the test, concrete is broken after the projectile penetration of the reinforced concrete slab, and complex interactions exist between the broken concrete. But in the numerical simulation, concrete does not interact with each other after failure; concrete is in a state of fragmentation and has no relation with each other in initial catering and shear plugging stages; (2) Concrete is a brittle material with low tensile strength, which causes the tensile stress wave generated by the stress wave to be reflected on the rear face of the concrete slab and to easily crush the concrete. However, in this study, the HJC concrete model uses the elastic-viscoplastic model to consider the tensile strength of concrete materials without considering the effects of tensile damage and strain rate. The numerical simulation of concrete splash smaller than the experimental value in the initial catering and shear plugging stages. In addition, in the numerical calculation of projectile penetration into the reinforced concrete slab, the focus is on the penetration depth, penetration resistance, penetration holes diameter, reinforcing bars deformation and its effect on penetration resistance. The shape of the initial catering and shear plugging area are not considered.

The numerical and experimental results of the reinforced concrete damage are shown in Fig. 13. A damage mark that enables display and evaluation of damage spread in concrete is added to the program. The damage of the front target of numerical simulation was smaller than that of the experimental results due to the continuity hypothesis. The damage area on the target back almost covered the whole concrete surface, which was consistent with the experimental results.

The numerical and experimental results of the reinforcing bar deformation are shown in Fig. 14. The reinforcing bars do not fracture in the numerical simulation but is bulged out in the radial direction with penetration and is consistent with the reinforcing bar deformation results in the experiments. The 3D data field of particles was output to observe the reinforcing bar deformation with penetration, as shown in Fig. 15.

5.2. Parameter analysis

5.2.1. Effect of the initial impact velocity of the projectile on penetration performance

Based on the numerical simulation in Section 5.1, we studied the residual velocity of the projectile perforation of concrete and reinforced concrete with different initial impact velocities. In this Section, the calculation mode, material parameters, and EOS are the same as those used in Section 5.1. The initial impact velocity in the simulation was set as 1200 m/s, 1300 m/s, 1400 m/s and 1500 m/s, respectively, to discuss the high impact velocity effect. The velocity-time curves of projectile penetration into concrete and reinforced concrete with different initial impact velocity are shown in Fig. 16. Velocity attenuation curves with different initial impact velocity are consistent, which indicate that the effects of initial impact velocity on concrete and reinforced concrete penetration are similar. The residual velocity of reinforced concrete penetration increases from 450 m/s to 580 m/s, and that of concrete penetration, from 550 m/s to 700 m/s, indicating that the reinforcing bars have obvious resistance to the projectile penetration process.

5.2.2. Effect of the concrete uniaxial compressive strength on penetration performance

The uniaxial compressive strength of concrete was set as 20 MPa, 40 MPa, 60 MPa, 80 MPa, and 100 MPa, respectively, in the simulation to study its effect on the penetration. The material parameters of the projectile and the size of the concrete slab in the simulation are consistent with those used in the experiment [4]. The EOS and material parameters of the reinforced concrete are consistent with those used in Section 5.1.

The projectile penetrated reinforced concrete target of a 1.0 m at an initial impact velocity of 1500 m/s, and the residual velocity versus uniaxial compressive strength of concrete is shown in Fig. 17. The residual velocity is reduced with increased uniaxial compressive strength, but the reduction degree was small, which is slightly inconsistent with the actual situation. This inconsistency may be caused by the continuity assumption. When the projectile impacted concrete with a high velocity, the concrete material entered the plastic state, which weakened the effect of yield limit to the penetration resistance, and thus decreased the effect of the uniaxial compressive strength on the residual velocity of the projectile perforation of reinforced concrete.

Fig. 14. Comparison of numerical results and experimental results of reinforcing bars.

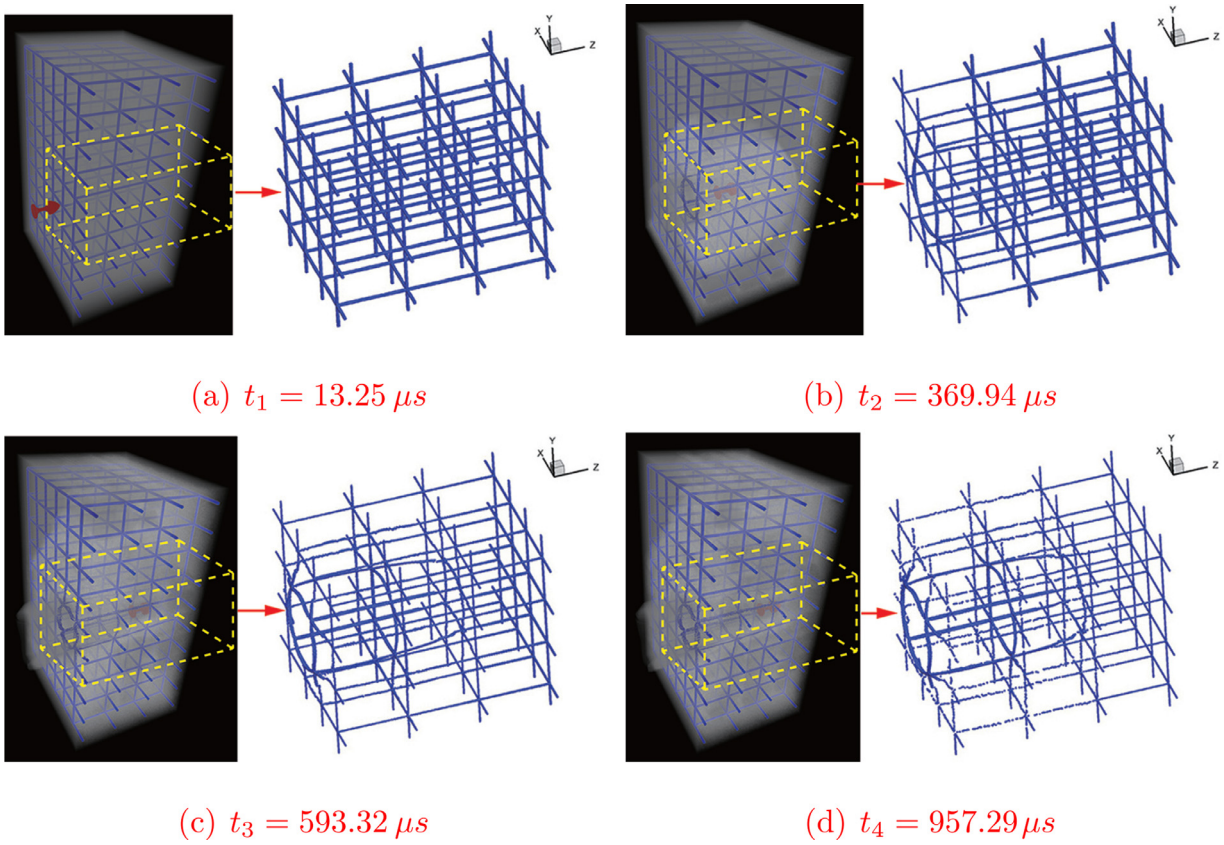

Fig. 15. Deformation process of reinforcing bars.

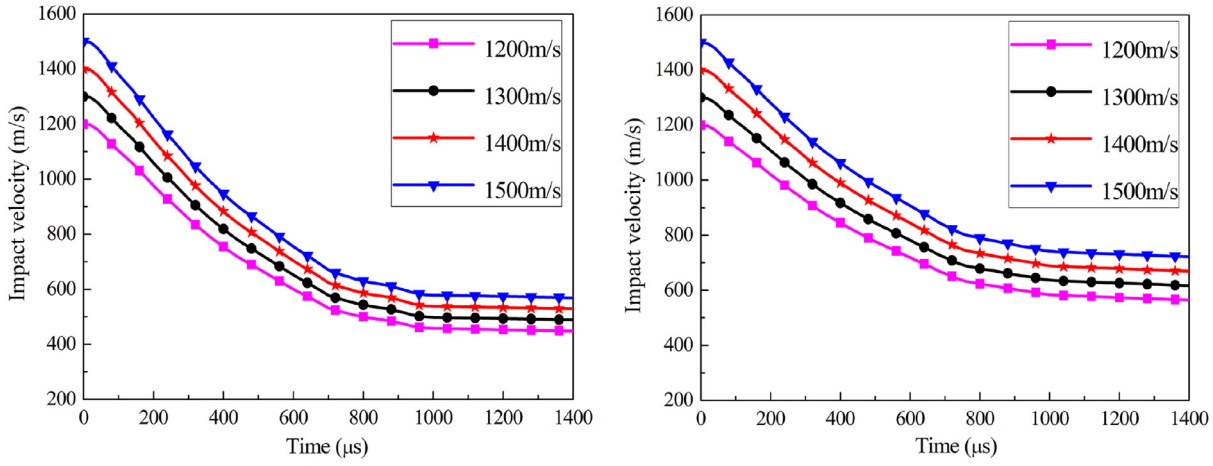

(a) Velocity-time curves of projectile penetration into concrete

(b) Velocity-time curves of projectile penetration into reinforced concrete

Fig. 16. Velocity-time curves of projectile penetration into concrete and reinforced concrete with different initial impact velocity.

5.2.3. Effect of the concrete slab thickness on penetration performance

In this part, the thicknesses of concrete are set as 1.0 m, 1.25 m, 1.5 m, and 1.75 m respectively, and all other conditions are the same as the Section 5.1. The velocity-time curves of projectile penetration into the different thickness of reinforced concrete with an initial impact velocity 1500 m/s are shown in Fig. 18. Four curves have the same trends and shapes. The velocity decreases steeply at the early stage and steadily at the last stage. Comparisons of the residual velocities of the projectile penetration into different slab thicknesses show that the slab thickness has an important effect on the penetration performance. The residual velocity decreases significantly with increased the target thickness.

6. Conclusion

In this study, the failure analysis of the reinforced concrete slab under impact loading was conducted using a 3D coupled Eulerian-Lagrangian method, which can solve the problem of multi-material

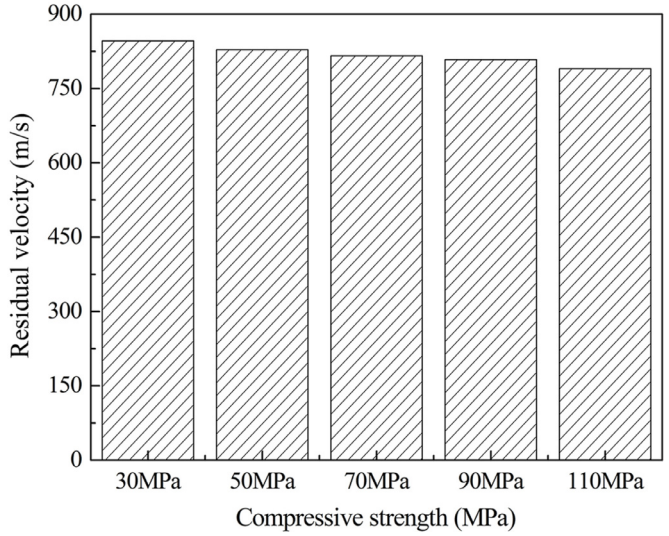

Fig. 17. Residual velocity versus concrete compressive strength at V = 1500 m/s.

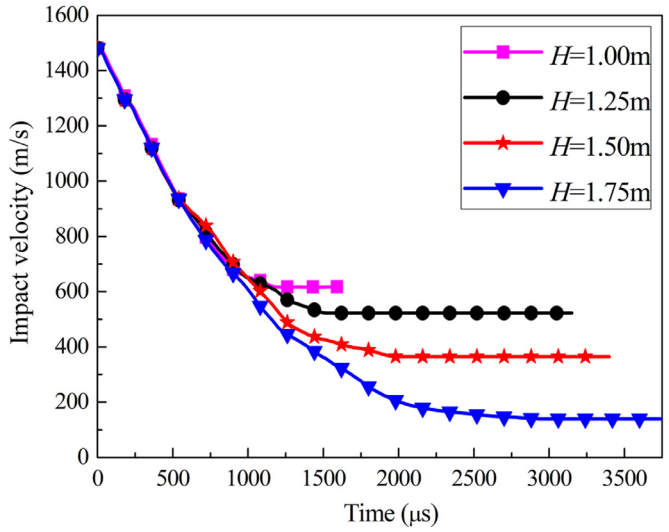

Fig. 18. Velocity-time curves of projectile penetration into the different slab thickness.

interface processing in the Eulerian method by adding the Lagrangian particles to the Eulerian background cells. The method overcomes numerical fluctuation because of finite Lagrangian particles. Furthermore, different materials do not embed by joining the fixed cell and single-valued mapping. This method not only inherits the advantages of Lagrangian method such as easy interface tracking, a simple algorithm, and easy implementation, but also decreases the number of particles effectively, shorten the computing time, and reduces the memory requirement even with higher calculation precision.

Numerical results of projectile penetration into the reinforced concrete slab are consistent with the experimental data and with the previous numerical results. The novel 3D Eulerian-Lagrangian method can effectively simulate projectile penetration into the reinforced concrete slab and can accurately tracks the deformation history of the reinforcing bars during the penetration. The velocity-time curves with different initial impact velocity are consistent; concrete and reinforced concrete have similar attenuation curves, and reinforcing bar bars provide resistance to the projectile penetration process. The residual velocity after projectile perforation of the reinforced concrete slab decrease with uniaxial compressive strength and thickness of concrete.

It should be pointed out that a credible and accurate materials model can more accurately describe the material behavior of concrete under different loading conditions. The numerical simulation results in this study are obtained based on the HJC model. As mentioned in Section 2.3, there are some shortcomings in the HJC model, in future research work, we will continue to study the modified HJC model and other constitutive models, and select the most suitable model to obtain better numerical results.

Author Statement

Author Statement We wish to submit a manuscript entitled ”Failure analysis of reinforced concrete slab under impact loading using a novel numerical method.” for publication in International Journal of Impact Engineering as a research paper. The authors for this work are Jianguo Ning, Fanlin Meng, Tianbao Ma, and Xiangzhao Xu. All correspondence regarding this manuscript should be directed to Xiangzhao Xu. Jianguo Ning and Xiangzhao Xu made substantial contributions to the conception and design of the work; Xiangzhao Xu and Fanlin Meng completed the implementation of the 3D coupled Eulerian-Lagrangian method; Jianguo Ning and Tianbao Ma completed the parallelization and testing of the 3D coupled Eulerian-Lagrangian method; Tianbao Ma and Fanlin Meng performed the numerical simulation of projectile penetration into the concrete slab and reinforced concrete slab; Jianguo Ning and Xiangzhao Xu performed the comparison of predicted results by the present method with other predicted results and experimental data. This manuscript has not been published or presented elsewhere in part or entirety and is not under consideration by another journal, and all authors have approved the submission of the manuscript. We have read and understood your journal’s policies, and we believe that neither the manuscript nor the study violates any of these. Thank you for your assistance and please do not hesitate to contact us should you have any questions. We look forward to hearing from you soon.

Declaration of Competing Interest

The authors declared that they have no conflicts of interest in this work. We declare that we do not have any commercial or associative interest that represents a conflict of interest in connection with the work submitted.

Acknowledgment

This work was supported by the National Natural Science Foundation of China (Grant Nos. 11902036, 11822203 and 11532012).

References

[1] Sherburn J, Roth M, Chen J-S, Hillman M. Meshfree modeling of concrete slab perforation using a reproducing kernel particle impact and penetration formulation. Int J Impact Eng 2015;86:96–110. https://doi.org/10.1016/j.ijimpeng.2015.07.009.
[2] Sliseris J, Korjakins A. Numerical modeling of the casting process and impact loading of a steel-fiber-reinforced high-performance self-compacting concrete. Constr Build Mater 2019;212:304–16.
[3] Liu J, Wu C, Li J, Su Y, Shao R, Liu Z, et al. Experimental and numerical study of reactive powder concrete reinforced with steel wire mesh against projectile penetration. Int J Impact Eng 2017;109. https://doi.org/10.1016/j.ijimpeng.2017.06.006.
[4] Xu X, Ma T, Ning J. Failure mechanism of reinforced concrete subjected to projectile impact loading. Eng Fail Anal 2018;96. https://doi.org/10.1016/j.engfailanal.2018.11.006.
[5] Liu J, Wu C, Chen X. Numerical study of ultra-high performance concrete under non-deformable projectile penetration. Constr Build Mater 2017;135:447–58. https://doi.org/10.1016/j.conbuildmat.2016.12.216.
[6] Ning J, Ma T, Fei G. Multi-material eulerian method and parallel computation for 3d explosion and impact problems. Int J Comput Methods 2014;11:1350079. https://doi.org/10.1142/S0219876213500795.
[7] Xue B, Le J-L. Simplified energy-based analysis of collapse risk of reinforced concrete buildings. Struct Saf 2016;63:47–58. https://doi.org/10.1016/j.strusafe.2016.07.003.

[8] Xu X, Ma T, Ning J. Failure analytical model of reinforced concrete slab under impact loading. Constr Build Mater 2019;223:679–91. https://doi.org/10.1016/j.conbuildmat.2019.07.008.

[9] Engen M, Hendriks M, Khler J, Overli J, ldstedt E. A quantification of the modelling uncertainty of non-linear finite element analyses of large concrete structures. Struct Saf 2017;64:1–8. https://doi.org/10.1016/j.strusafe.2016.08.003.

[10] Wu C, Wu Y, Crawford J, Magallanes J. Three-dimensional concrete impact and penetration simulations using the smoothed particle galerkin method. Int J Impact Eng 2017;106. https://doi.org/10.1016/j.ijimpeng.2017.03.005.

[11] grdh L, Laine L. 3D fe-simulation of high-velocity fragment perforation of reinforced concrete slabs. Int J Imp Eng 1999;22:911–22. https://doi.org/10.1016/S0734-743X(99)00008-1.

[12] Huang F, Wu H, Jin Q, Zhang Q. A numerical simulation on the perforation of reinforced concrete targets. Int J Impact Eng 2005;32:173–87. https://doi.org/10.1016/j.ijimpeng.2005.05.009.

[13] Tham C. Numerical and empirical approach in predicting the penetration of a concrete target by an ogive-nosed projectile. Finite Elem Anal Des 2006;42:1258–68. https://doi.org/10.1016/j.finel.2006.06.011.

[14] Kapahi A, Sambasivan S, Udaykumar H. A three dimensional sharp interface cartesian grid method for solving high speed multi-material impact problems. J Comput Phys 2013;241:308–32. https://doi.org/10.1016/j.jcp.2013.01.007.

[15] Wang J, Gadala M. Formulation and survey of ale method in nonlinear solid mechanics. Finite Elem Anal Des 1997;24:253–69. https://doi.org/10.1016/S0168-874X(96)00061-3.

[16] Sulsky D, Chen Z, Schreyer H. A particle method for history-dependent materials. Comput Methods Appl Mech Eng 1994;118:179–96. https://doi.org/10.1016/0045-7825(94)90112-0.

[17] Liu P, Liu Y, Zhang X. Internal-structure-model based simulation research of shielding properties of honeycomb sandwich panel subjected to high-velocity impact. Int J Impact Eng 2015;77:120–33. https://doi.org/10.1016/j.ijimpeng.2014.11.004.

[18] Zhang X, Sze K. An explicit material point finite element method for hyper-velocity impact. Int J Numer Methods Eng 2006;66:689–706. https://doi.org/10.1002/nme.1579.

[19] He N, Liu Y, Zhang X. Seamless coupling of molecular dynamics and material point method via smoothed molecular dynamics. Int J Numer Methods Eng 2017. https://doi.org/10.1002/nme.5543.

[20] Ma T, Wang J, Ning J. A hybrid vof and pic multi-material interface treatment method and its application in the penetration. Sci China-Phys Mech Astron 2010;53:209–17. https://doi.org/10.1007/s11433-009-0263-2.

[21] Ren H, Ma T, Yao X. Numerical studies of penetration problems by an improved particle method. Sci China Phys Mech Astron 2012;55. https://doi.org/10.1007/s11433-012-4948-6.

[22] Attaway S, Heinstein M, Swegle J. Coupling of smooth particle hydrodynamics with the finite element method. Nucl Eng Des 1994;150:199–205. https://doi.org/10.1016/0029-5493(94)90136-8.

[23] Drathi R, Das A, Rangarajan A. Meshfree simulation of concrete structures und impact loading. Int J Impact Eng 2016;91. https://doi.org/10.1016/j.ijimpeng.2015.10.013.

[24] Sherburn J, Roth M, Chen J-S, Hillman M. Meshfree modeling of concrete slab perforation using a reproducing kernel particle impact and penetration formulation. Int J Impact Eng 2015;86:96–110. https://doi.org/10.1016/j.ijimpeng.2015.07.009.

[25] Wu C, Wu Y, Crawford J, Magallanes J. Three-dimensional concrete impact and penetration simulations using the smoothed particle galerkin method. Int J Impact Eng 2017;106. https://doi.org/10.1016/j.ijimpeng.2017.03.005.

[26] Ning J. Fuzzy interface treatment in eulerian method. Sci China Ser E Technol Sci 2004;47:550–68. https://doi.org/10.1360/03ye0451.

[27] Dannemann KA, Chalivendra VB, B. S. Fourth tms symposium on the dynamic behavior of materials: part ii (part i was published in november 2007.). Metallurgical and Materials Transactions A-physical Metallurgy and Materials Science - METALL MATER TRANS A 2007;38:2859–60. https://doi.org/10.1007/s11661-007-9408-y.

[28] Johnson G, Stryk R, Beissel S, Holmquist T. An algorithm to automatically convert distorted finite elements into meshless particles during dynamic deformation. Int J Imp Eng 2002;27:997–1013. https://doi.org/10.1016/S0734-743X(02)00030-1.

[29] Dawson A, Bless S, Levinson S, Pedersen B, Satapathy S. Hypervelocity penetration of concrete. Int J Imp Eng 2008;35:1484–9. https://doi.org/10.1016/j.ijimpeng.2008.07.069.

[30] Holmquist T.J. Johnson G.R.. Cook W.H. A computational constitutive model for concrete subjected to large strains, high strain rates and high pressures. In: Proceedings of 14th international symposium on Ballistics, Quebec, Canada1993;:591–600.

[31] Polanco-Loria M, Hopperstad O, Brvik T, Berstad T. Numerical predictions of ballistic limits for concrete slabs using a modified version of the hjc concrete model. Int J Impact Eng 2008;35:290–303. https://doi.org/10.1016/j.ijimpeng.2007.03.001.

[32] Liu Y, Ma A, Huang F. Numerical simulation of oblique-angle penetration by deformable projectile into concrete target. Int J Imp Eng 2009;36:438–46. https://doi.org/10.1016/j.ijimpeng.2008.03.006.

[33] Islam M, Swaddiwudhipong S, Liu Z. Penetration of concrete targets using a modified holmquist-johnson-cook material model. Int J Comput Methods 2013;9. https://doi.org/10.1142/S0219876212500569.

[34] Kong X, Fang Q, Wu H, Peng Y. Numerical predictions of cratering and scabbing in concrete slabs subjected to projectile impact using a modified version of hjc material model. Int J Impact Eng 2016;95. https://doi.org/10.1016/j.ijimpeng.2016.04.014.

[35] xu H, Wen H. Semi-empirical equations for the dynamic strength enhancement of concrete-like materials. Int J Impact Eng 2013;60:76–81. https://doi.org/10.1016/j.ijimpeng.2013.04.005.

[36] xu H, Wen H. A computational constitutive model for concrete subjected to dynamic loadings. Int J Impact Eng 2016;91. https://doi.org/10.1016/j.ijimpeng.2016.01.003.

[37] Xu L, xu H, Wen H. On the penetration and perforation of concrete targets struck transversely by ogival-nosed projectiles - a numerical study. Int J Impact Eng 2019;125:39–55. https://doi.org/10.1016/j.ijimpeng.2018.11.001.

[38] Beissel S, Johnson G. Abrasion algorithm for projectile mass loss during penetration. Int J Imp Eng 2000;24:103–16. https://doi.org/10.1016/S0734-743X(99)00146-3.

[39] Hu F, Wu H, Fang Q, Liu J. Impact resistance of concrete targets pre-damaged by explosively formed projectile (efp) against rigid projectile. Int J Impact Eng 2018;122. https://doi.org/10.1016/j.ijimpeng.2018.08.014.

[40] Peng Y, Wu H, Fang Q, Gong Z. Geometrical scaling effect for penetration depth of hard projectiles into concrete targets. Int J Impact Eng 2018;120. https://doi.org/10.1016/j.ijimpeng.2018.05.010.

[41] Zhang J, Hao H, Wang Z, Wang Z, Shu X. Performance of concrete targets mixed with coarse aggregates against rigid projectile impact. Int J Impact Eng 2020;141:103565. https://doi.org/10.1016/j.ijimpeng.2020.103565.

[42] Heng D, Liu Z, Wu H, Gao X, Pi A, Huang F. Study on penetration characteristics of high-speed elliptical cross-sectional projectiles into concrete. Int J Impact Eng 2019;132. https://doi.org/10.1016/j.ijimpeng.2019.05.025.

[43] Wu H, Li Y, Fang Q, Peng Y. Scaling effect of rigid projectile penetration into concrete target: 3d mesoscopic analyses. Constr Build Mater 2019;208:506–24. https://doi.org/10.1016/j.conbuildmat.2019.03.040.

[44] Liu J, Aiguo P, Huang F. Penetration performance of double-ogive-nose projectiles. Int J Impact Eng 2015;84. https://doi.org/10.1016/j.ijimpeng.2015.05.003.

[45] Ren G-M, Wu H, Fang Q, Kong X. Parameters of holmquist-johnson-cook model for high-strength concrete-like materials under projectile impact. International Journal of Protective Structures 2017;8. https://doi.org/10.1177/2041419617721552.204141961772155

[46] Hirt C, Nichols B. Volume of fluid (vof) method for the dynamics of free boundary. J Comput Phys 1981;39. https://doi.org/10.1016/0021-9991(81)90145-5.

[47] Rider W, Kothe D. Reconstructing volume tracking. J Comput Phys 1999;141. https://doi.org/10.1006/jcph.1998.5906.

[48] Osher S, Fedkiw R. Level set methods: an overview and some recent results. J Comput Phys 1970;169:463–502. https://doi.org/10.1006/jcph.2000.6636.

[49] Forrestal M, Frew D, Hickerson J, Rohwer T. Penetration of concrete targets with deceleration-time measurement. Int J Imp Eng 2003;28:479–97. https://doi.org/10.1016/S0734-743X(02)00108-2.

[50] Frew D, Forrestal M, Cargile J. The effect of concrete target diameter on projectile deceleration and penetration depth. Int J Impact Eng 2006;32:1584–94. https://doi.org/10.1016/j.ijimpeng.2005.01.012.

[51] Chen R, Han X, Liu J, Zhang W. A computational inverse technique to determine the dynamic constitutive model parameters of concrete. Comput Mater Continua 2011;25:135–57.

[52] Kennedy R. A review of procedures for the analysis and design of concrete structures to resist missile impact effects. Nucl Eng Des 1976;37:183–203. https://doi.org/10.1016/0029-5493(76)90015-7.

[53] Forrestal M, Altman B, Cargile J, Hanchak S. An empirial equation for penetration depth of ogive-nose projectiles into concrete targets. Int J Imp Eng 1994;15:395–405. https://doi.org/10.1016/0734-743X(94)80024-4.

[54] Warren T, Fossum A, Frew D. Penetration into low-strength (23mpa) concrete: target characterization and simulations. International Journal of Impact Engineering 2004;30(5):477–503. https://doi.org/10.1016/S0734-743X(03)00092-7. http://www.sciencedirect.com/science/article/pii/S0734743X03000927

[55] Ning J, Ma T, Lin G. A grid generator for 3-d explosion simulations using the staircase boundary approach in cartesian coordinates based on stl models. Adv Eng Software 2014;67:148–55. https://doi.org/10.1016/j.advengsoft.2013.09.007.